Shortwave infrared fluorescence imaging with the clinically approved near-infrared dye indocyanine green

Jessica A. Carr[a,1], Daniel Franke[a,1], Justin R. Caram[a,2], Collin F. Perkinson[a], Mari Saif[a], Vasileios Askoxylakis[b], Meenal Datta[b,c], Dai Fukumura[b], Rakesh K. Jain[b], Moungi G. Bawendi[a,3], and Oliver T. Bruns[a,3,4]

[a]Department of Chemistry, Massachusetts Institute of Technology, Cambridge, MA 02139; [b]Edwin L. Steele Labs for Tumor Biology, Department of Radiation Oncology, Massachusetts General Hospital, MGH Research Institute and Harvard Medical School, Boston, MA 02114; and [c]Department of Chemical and Biological Engineering, Tufts University, Medford, MA 02155

Contributed by Moungi G. Bawendi, March 7, 2018 (sent for review November 2, 2017; reviewed by Frauke Alves and Ute Resch-Genger)

Fluorescence imaging is a method of real-time molecular tracking in vivo that has enabled many clinical technologies. Imaging in the shortwave IR (SWIR; 1,000–2,000 nm) promises higher contrast, sensitivity, and penetration depths compared with conventional visible and near-IR (NIR) fluorescence imaging. However, adoption of SWIR imaging in clinical settings has been limited, partially due to the absence of US Food and Drug Administration (FDA)-approved fluorophores with peak emission in the SWIR. Here, we show that commercially available NIR dyes, including the FDA-approved contrast agent indocyanine green (ICG), exhibit optical properties suitable for in vivo SWIR fluorescence imaging. Even though their emission spectra peak in the NIR, these dyes outperform commercial SWIR fluorophores and can be imaged in the SWIR, even beyond 1,500 nm. We show real-time fluorescence imaging using ICG at clinically relevant doses, including intravital microscopy, noninvasive imaging in blood and lymph vessels, and imaging of hepatobiliary clearance, and show increased contrast compared with NIR fluorescence imaging. Furthermore, we show tumor-targeted SWIR imaging with IRDye 800CW-labeled trastuzumab, an NIR dye being tested in multiple clinical trials. Our findings suggest that high-contrast SWIR fluorescence imaging can be implemented alongside existing imaging modalities by switching the detection of conventional NIR fluorescence systems from silicon-based NIR cameras to emerging indium gallium arsenide-based SWIR cameras. Using ICG in particular opens the possibility of translating SWIR fluorescence imaging to human clinical applications. Indeed, our findings suggest that emerging SWIR-fluorescent in vivo contrast agents should be benchmarked against the SWIR emission of ICG in blood.

shortwave infrared | biomedical imaging | fluorescence imaging | near infrared | indocyanine green

Fluorescence imaging in the near-IR (NIR; 700–1,000 nm) has enabled new technologies for a large variety of preclinical and clinical applications (1–5). Compared with conventional diagnostic imaging, such as computed tomography, positron emission tomography, or magnetic resonance imaging, NIR fluorescence imaging provides a lower-cost, high-sensitivity method for real-time molecular imaging (2, 3, 5). A variety of NIR fluorophores are commercially available, exhibit high brightness, and can target a range of biological substrates. Moreover, one of these dyes, indocyanine green (ICG), has been approved by the US Food and Drug Administration (FDA) for clinical use since 1959. ICG and other NIR dyes, such as IRDye 800CW, are the subject of over 300 clinical trials for applications like fluorescence angiography and perfusion assessment in reconstructive and bypass surgeries, metastatic lymph node mapping and lymphatic transport tracking in lymphedema, cancer localization and surgical margin assessment, and many others (4–11).

Recent research has shown that extending fluorescence imaging into shortwave IR (SWIR; 1,000–2,000 nm) wavelengths can further enhance the advantages of NIR imaging (12–15). Low levels of background tissue autofluorescence in the SWIR increase imaging sensitivity to a target fluorophore, and the unique tissue absorption and scattering properties increase contrast of structures at greater penetration depths compared with fluorescence imaging in the NIR (13, 16–21). However, the adoption of SWIR fluorescence imaging into clinical settings has been prevented by the limited availability of SWIR detection technology and the perceived need for FDA-approved fluorophores with peak emission in the SWIR spectral region. The availability of SWIR detectors, controlled in part by national defense-related policies, such as the US International Traffic in Arms Regulations, is rapidly increasing, as over 20 SWIR cameras are now classified for dual (military and commercial) use by the US Department of State (22). In addition, improvements in indium gallium arsenide (InGaAs) sensor fabrication, increasing supply, and growing markets have significantly decreased SWIR detection technology costs (23). As for SWIR-fluorescent probes,

Significance

Imaging in the shortwave IR (SWIR) spectral window allows the observation of processes deep within living animals. Recent studies have shown that SWIR imaging enables unprecedented imaging opportunities, including contact-free monitoring of vital signs, generation of microvasculature blood flow maps, real-time metabolic imaging, and molecularly targeted imaging. Yet, whereas bright SWIR fluorophores have been developed for preclinical research settings, applications in the clinic have been held back by the conventional belief that no clinically approved fluorophore is available. Here, we show that indocyanine green, a clinically approved near-IR dye, exhibits a remarkable amount of SWIR emission, which enables state-of-the-art SWIR imaging with direct translation potential into clinical settings, and even outperforms other commercially available SWIR emitters.

Author contributions: J.A.C., D. Franke, J.R.C., D. Fukumura, R.K.J., M.G.B., and O.T.B. designed research; J.A.C., D. Franke, J.R.C., C.F.P., M.S., V.A., M.D., and O.T.B. performed research; J.A.C., D. Franke, J.R.C., C.F.P., M.S., V.A., M.D., D. Fukumura, R.K.J., and O.T.B. contributed new reagents/analytic tools; J.A.C., D. Franke, J.R.C., C.F.P., M.S., V.A., M.G.B., and O.T.B. analyzed data; and J.A.C., D. Franke, M.G.B., and O.T.B. wrote the paper.

Reviewers: F.A., University of Göttingen; and U.R.-G., Federal Institute for Materials Research and Testing.

The authors declare no conflict of interest.

[1]J.A.C. and D. Franke contributed equally to this work.

[2]Present address: Department of Chemistry and Biochemistry, University of California, Los Angeles, CA 90095.

[3]To whom correspondence may be addressed. Email: mgb@mit.edu or oliver.bruns@helmholtz-muenchen.de.

[4]Present address: Helmholtz Pioneer Campus, Helmholtz Zentrum München, D-85764 Neuherberg, Germany.

This article contains supporting information online at www.pnas.org/lookup/suppl/doi:10.1073/pnas.1718917115/-/DCSupplemental.

Published online April 6, 2018.

several examples of inorganic nanomaterials and hydrophobic organic molecules exist with peak emission in the SWIR. Increasing the quantum yield, functionality, and biocompatibility of SWIR fluorophores is an active focus of emerging research studies (24–41).

Here, we show that two commercially available dyes with peak emission in the NIR spectral region, including the FDA-approved contrast agent ICG, can function as SWIR emitters. Indeed, despite having emission that peaks in the NIR, these dyes outperform commercial SWIR fluorophores with peak emission in the SWIR. Our findings are based on the observation that, although the emission spectrum of NIR dyes, such as ICG or IRDye 800CW, peaks outside of the SWIR spectral region, their fluorescence spectrum exhibits a broad shoulder with a spectral tail extending well into the SWIR that can be easily detected by modern SWIR cameras. Furthermore, dyes, such as ICG, have extinction coefficients at their absorption peak that far exceed those of some existing SWIR fluorophores. By showing both functional and targeted SWIR imaging, our findings suggest that NIR dyes could bridge the gap between current shortcomings of SWIR fluorescent probes and applications in clinical settings. Indeed, our findings suggest that any emerging SWIR-fluorescent in vivo contrast agent should be benchmarked against the SWIR emission of ICG in blood.

Results and Discussion

NIR Dye Emission Detected with InGaAs. The visible and NIR emission properties of fluorescent materials are commonly characterized using ubiquitous silicon-based detection technology and spectrometers. However, the detection efficiency of these detectors sharply declines beyond 900 nm, making calibration beyond this wavelength challenging and often limiting detection of the full spectrum of materials with NIR emission. The emission spectrum of ICG reported in many of ~3,000 published papers and by dye manufacturers, for example, underrepresents the extent of its NIR and SWIR emission (refs. 42, 43; https://www.accessdata.fda.gov/scripts/cder/daf/index.cfm?event=overview.process&applno=011525). This often originates from recording the emission spectra of NIR dyes on improperly calibrated silicon-based detectors, including some commercial spectrometer systems (Fig. S1*A*).

Recording the emission spectra on a system sensitive to both NIR and SWIR light, such as an InGaAs detector-based system, shows that ICG emission extends well into the SWIR region (Fig. 1) (44).

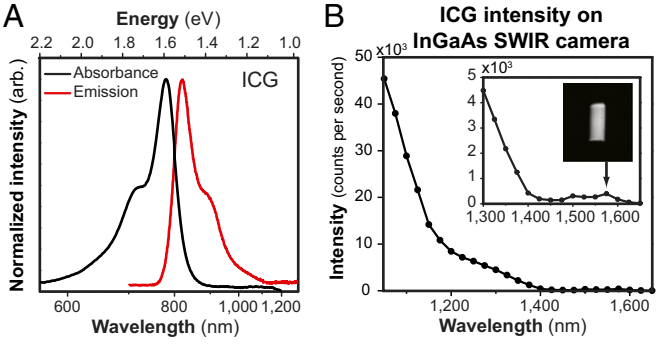

Fig. 1. SWIR emission of the NIR dye ICG. (*A*) The full emission spectrum of ICG, measured on an NIR- and SWIR-sensitive InGaAs detector (red line), mirrors the absorption spectrum (black line) as predicted by the Franck–Condon principle. (*B*) The emission intensity of a 0.027 mg/mL aqueous ICG solution, detected in 20-nm spectral bands on an InGaAs camera and normalized by integration time, shows that emission is detectable up to at least 1,575 nm (*Inset* shows the vial). A lower intensity is observed between 1,400 and 1,500 nm due to the absorption band of water at those wavelengths.

We show that, with all corrections performed by us (Fig. S1), the emission spectrum of ICG approximates the mirror image of its absorption spectrum as predicted by the Franck–Condon principle (or mirror image rule) (45). Furthermore, we show that, under diffuse 808-nm excitation, it is even possible to detect emission from an aqueous solution of ICG on an InGaAs SWIR camera beyond 1,500 nm, although the emission of ICG peaks at 820 nm. This finding is significant in the context of recent studies showing the improvement in contrast, sensitivity, and penetration that can be gained by performing fluorescence imaging at the longest wavelengths of the SWIR (12–14). The same principle applies not only to ICG but also, to other NIR dyes, such as IRDye 800CW (Fig. S1*B*), which is currently in multiple phase II clinical trials and promises improved stability compared with ICG (46).

In fact, the SWIR emission from NIR dyes, such as ICG and IRDye 800CW, exceeds the brightness of a commercially available, state of the art organic fluorophore developed specifically for in vivo SWIR imaging applications (IR-E1050). The underlying reasons for this finding become evident by comparing the optical properties of aqueous ICG and IRDye 800CW with those of IR-E1050, which has peak emission in the SWIR (Fig. 2) (www.nirmidas.com/nirii-dye/). The brightness of a fluorescent probe is given by the product of the fluorescence quantum yield with the probe's absorption cross-section at the excitation wavelength. ICG and IRDye 800CW exhibit both higher quantum yields in aqueous solutions (0.9 and 3.3%, respectively) and higher peak absorption cross-sections (15×10^4 and 24×10^4 M^{-1} cm^{-1}, respectively) than IR-E1050 (quantum yield of 0.2%, peak absorption cross-section of 0.80×10^4 M^{-1} cm^{-1}) (47–50). Thus, when normalized to equimolar concentrations in water, we measure the emission intensity of ICG between 1,000 and 1,300 nm to be 8.7 times higher than that of IR-E1050 (Fig. 2 *A*–*C*). Indeed, simply using the absorption cross-section, quantum yield, and the ratio of the number of photons emitted between 1,000 and 1,300 nm to the total number of emitted photons (5% for ICG and 47% for IR-E1050) predicts that ICG should be 9.1 times brighter that IR-E1050, consistent with our measurements (Fig. 2*D*). The superior brightness of ICG compared with IR-E1050 in the SWIR is indeed apparent when comparing the brightness from vials of the two dyes on the InGaAs camera that we subsequently use for our in vivo imaging (Fig. S2 *A* and *B*).

We further compare the emission intensities of ICG, IRDye 800CW, and IR-E1050 in bovine blood on an InGaAs camera to best estimate the in vivo brightness of the probes (Fig. 2 *E* and *F*). It is important that a full characterization includes a comparison in blood, as characterization in water underrepresents the in vivo brightness of ICG due to (*i*) formation of H-dimer species at low concentrations in water that cause fluorescence quenching and (*ii*) the association of ICG with albumin and other proteins in blood that stabilizes the dye and increases its quantum yield (6, 44). To quantify the molar brightness of the probes on the camera, the intensity of each vial containing equal masses of the respective dye was measured individually, averaged, and normalized to integration time and molecular concentration of the respective dye. In blood, equimolar ICG and IRDye 800CW were 16 and 1.3 times brighter, respectively, than IR-E1050 in the wavelength range from 1,300 to 1,620 nm when excited with 808-nm light.

We further confirm these results with in vivo SWIR imaging (Fig. S2 *C* and *D* and Movie S1), which shows that ICG is at least one order of magnitude brighter than IR-E1050 when imaging beyond 1,000 nm, in good agreement with the in vitro comparison.

Thus, commercially available and clinically relevant NIR fluorophores have significant SWIR emission, eliminating one of the barriers to adopting SWIR fluorescence imaging in both research and clinical applications. These results further emphasize that the selection of contrast agents for SWIR fluorescence imaging is not limited to probes with peak emission in the SWIR.

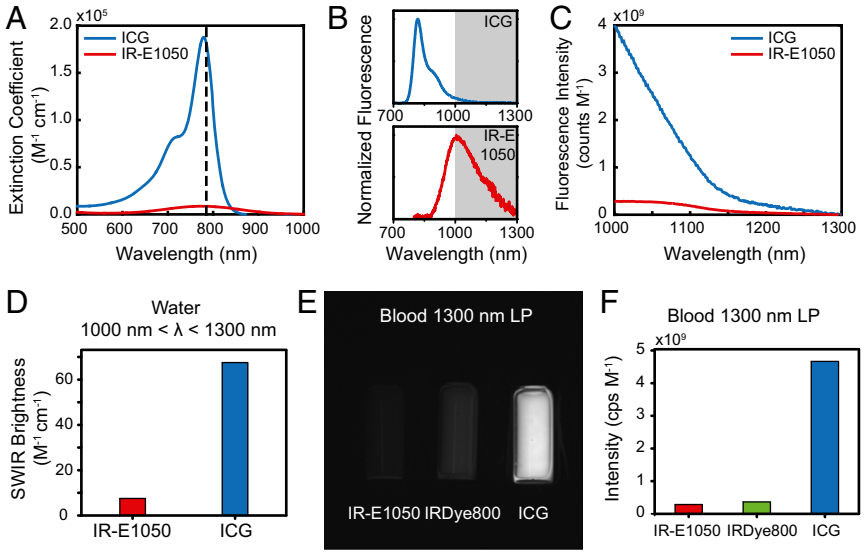

Fig. 2. Comparison of the optical properties of ICG with those of other NIR and SWIR dyes. (*A*) Normalized to identical molar concentrations, ICG absorbs much stronger at 785-nm excitation (dashed line) than IR-E1050, a commercially available SWIR dye marketed for in vivo SWIR imaging applications. (*B*) Thus, although the emission peak of ICG is significantly blue shifted compared with IR-E1050, (*C*) the measured emission intensity between 1,000 and 1,300 nm normalized to equimolar concentration is 8.7 times higher for ICG than for IR-E1050. (*D*) This finding was confirmed by calculating the SWIR brightness of ICG and IR-E1050 at wavelengths between 1,000 and 1,300 nm. Multiplying the independently measured fluorescence quantum yield, the maximum absorption cross-section, and the ratio of the number of photons emitted between 1,000 and 1,300 nm to the total number of emitted photons of both dyes shows that ICG is roughly nine times brighter than IR-E1050. (*E*) We further compared the fluorescence intensity of IR-E1050 (0.01 mg/mL) with that of IRDye 800CW PEG (0.01 mg/mL; not accounting for PEG shell of 25–60 kDa) and that of ICG (0.01 mg/mL) in bovine blood on an SWIR camera with a 1,300-nm long-pass (LP) filter. (*F*) Normalized to equimolar concentrations, the imaged intensity of the NIR dyes is greater than IR-E1050. SDs for signal intensity were found to be less than 5%. Fig. S2 and Movie S1 show comparisons in water and in vivo.

Due to the low quantum yields and low absorption cross-sections of conventional SWIR fluorophores, it is possible for the brightest probe to be one with only tail emission in the SWIR. Any SWIR-fluorescent contrast agent should, therefore, be benchmarked against the SWIR emission of ICG in blood, as it is sufficiently bright for in vivo applications, and it is already FDA approved and clinically used.

High-Contrast SWIR Fluorescence Imaging in Vivo Using ICG. The SWIR emission of commercially available, FDA-approved, and clinically used ICG enables straightforward application to in vivo fluorescence imaging in the SWIR. We present here a selection of in vivo imaging applications in mice using the clinically approved dose of ICG and highlight advantages of imaging ICG using SWIR detection over conventional NIR detection.

We show that imaging ICG in the SWIR enables high-contrast mesoscopic imaging of brain and hind-limb vasculature in mice through intact skin (Fig. 3), as has been previously shown with carbon nanotubes (13). For this, we injected an aqueous solution of ICG into the tail vein of mice at a dose of 0.2 mg/kg, which is within the recommended dose for humans (0.2–0.5 mg/kg recommended, 5 mg/kg maximum) (6). We illuminated the mice with 50–70 mW/cm^2 of 808-nm excitation light, staying below the maximum permissible exposure limit (330 mW/cm^2 for 808-nm continuous wave light) (51). We noninvasively imaged the resulting fluorescence on a silicon camera at NIR wavelengths and on an InGaAs camera at SWIR wavelengths between 1,300 and 1,620 nm, the detection cutoff of the cooled SWIR camera. We chose the 1,300- to 1,620-nm wavelength range, since as we show here and others have previously shown, contrast and resolution are maximized at wavelengths greater than 1,300 nm (13, 19, 52). We quantified the contrast within a region of interest in the NIR image and the SWIR image by calculating the coefficient of variation, defined as the standard deviation (SD) of pixel intensity normalized to the mean pixel intensity (Fig. S3*D*). We find that the SWIR image contrast for brain vasculature is nearly 50% greater at a value of 0.29 compared with the NIR image with a contrast value of 0.20, and it is more than 58% greater for hind-limb vasculature at a value of 0.19 for SWIR imaging compared with 0.12 for NIR imaging. Furthermore, we calculated the apparent width of a brain vessel by measuring the FWHM of a two-Gaussian fit to the intensity profile across the brain vessel of interest (Fig. S3*E*). We find that the apparent vessel width in this specific example is over twice as wide in the NIR image as in the SWIR image, with values of 430 and 210 μm, respectively. These findings are in good agreement with previous studies using other fluorophores (e.g., the contrast and resolution of brain vessels originally shown through noninvasive imaging using SWIR-emissive carbon nanotubes) (13). Thus, contrast and resolution of fine vasculature structures can be greatly improved while using FDA-approved ICG contrast by simply switching the detection wavelength from traditional NIR imaging using a silicon camera to detection beyond 1,300 nm on an InGaAs SWIR camera.

We further show that the contrast improvement of SWIR detection over NIR detection can be enabling for intravital microscopic imaging (Fig. S4). We incorporated ICG into PEG phospholipids (53) to increase its blood half-life, which is typically limited to 3–4 min (54, 55). We injected an aqueous solution of these micelles at a dose of 5 mg ICG/kg mouse into the tail vein of a mouse with an implanted cranial window and used a microscope to image the fluorescence of the ICG phospholipid micelles in the brain vasculature with both NIR and 1,300-nm long-pass SWIR detection. Images of the entire cranial window at 2× magnification show the ability to resolve nearly all of the same vessels using either NIR or SWIR imaging. The overall contrast, however, was 1.4 times greater for the SWIR image (SD/mean was 0.24 for NIR vs. 0.33 for SWIR). Higher magnification (6×) reveals that this contrast improvement using SWIR imaging enables the resolution of vessels, which due to the high

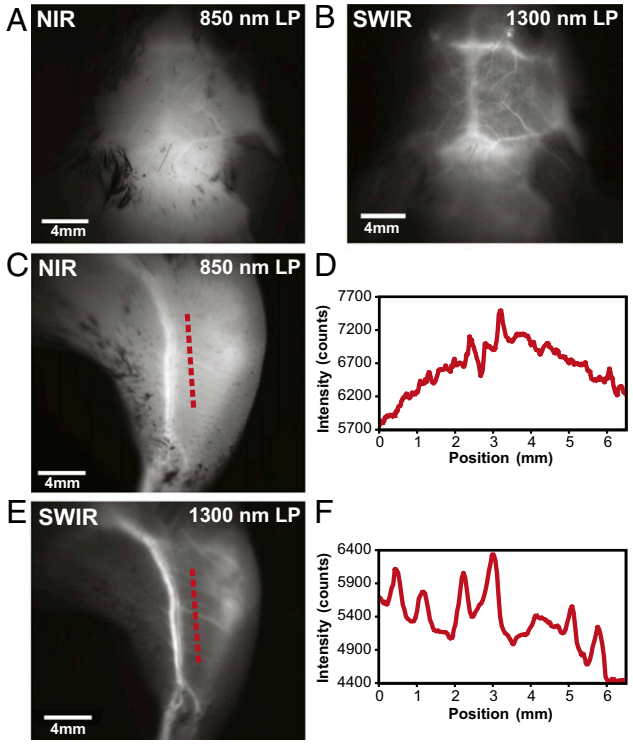

Fig. 3. High contrast in vivo SWIR fluorescence imaging using ICG. (*A*) We noninvasively imaged the brain vasculature of a mouse using ICG contrast and find that the vessels are difficult to resolve through skin and skull using 850-nm long-pass (LP) NIR detection on a silicon camera. (*B*) Switching to 1,300-nm long-pass SWIR detection on an InGaAs camera greatly improves vessel contrast (Fig. S3 shows contrast quantification). (*C*) Similarly, only large hind-limb vessels are imaged with good contrast through the skin using NIR detection. (*D*) The intensity across a line of interest shows insufficient contrast to resolve smaller vessels from background signal. (*E*) Using 1,300-nm long-pass SWIR detection greatly improves image contrast and (*F*) resolution of vessels. All images were scaled to the maximum displayable intensities.

label density of surrounding vessels, are difficult to distinguish from background signal in the NIR image.

These findings could improve clinical use of ICG in fluorescence angiography. Clinical imaging of ICG in the NIR has already shown value for angiography in ophthalmology, intraoperative assessment of blood vessel patency in tissue graft, bypass surgeries, and intracranial aneurism surgeries (1, 5, 56–59). Noninvasive imaging of lymphatic vasculature using ICG has also been described for surgical mapping and intraoperative identification of sentinel nodes, imaging nodes following surgical excision, and evaluation and monitoring of lymphedema (1, 5, 60, 61). Increasingly, ICG fluorescence imaging is also being used in robot-assisted surgery, in which the surgeon relies on visual cues instead of tactile feedback (7, 11, 61). However, full clinical implementation has been partially limited by insufficient image quality in deep operating fields. The higher contrast of ICG SWIR fluorescence imaging over NIR imaging could benefit these applications and enable resolution of finer vessels, especially in applications with high label density or interfering background signal. Importantly, the implementation of this contrast improvement would be straightforward, requiring only a switch from cameras with NIR sensitivity to those with SWIR sensitivity while continuing the familiar surgical setup and use of ICG.

Real-Time SWIR Fluorescence Imaging Using ICG. An essential component of fluorescence-guided surgery is the ability to perform real-time imaging. We show that the SWIR emission of ICG is sufficiently bright for real-time imaging at high frame rates using clinically approved doses of ICG. In one example, we performed heart angiography in mice. Using diffuse 808-nm excitation and a 1,300-nm long-pass emission filter, we were able to image the vasculature of a beating heart intravitally at a speed of 9.17 frames per second (Movie S2) while resolving fine vessels on the exterior surface against the underlying contrast (Fig. S5*E*). The acquisition speed was sufficiently fast to capture the anesthetized mouse heart rate of 207 beats per minute determined by tracking the intensity fluctuations of the heart (Fig. 4). Furthermore, the fluorescence of the ICG bolus was tracked as it reached the heart, lungs, peripheral veins, and finally, liver (Fig. S5 *A*–*D*).

In a second example, we show real-time SWIR imaging of ICG in the liver and small intestine of a mouse and further show imaging of ICG fluorescence beyond 1,500 nm. After ICG injection into the tail vein of a mouse, we noninvasively imaged through the skin the hepatobiliary excretion of ICG into the small intestine (6). ICG emitted sufficient signal for near-video rate imaging (19.7 frames per second, 1,200-nm long-pass filter), enabling capture of the peristaltic movements of the small intestine (Movie S3). Although at the cost of speed (2.0 frames per second), it was even feasible to image the ICG clearance using a 1,500-nm long-pass filter, capturing wavelengths between roughly 1,500 and 1,620 nm (Fig. S6*A*).

In a third example, we noninvasively imaged lymphatic flow in mice. We injected an aqueous solution of ICG s.c. in the hind feet and the tail and then imaged (at 9.17 frames per second through intact skin) the flow of lymphatic clearance (Movies S4 and S5).

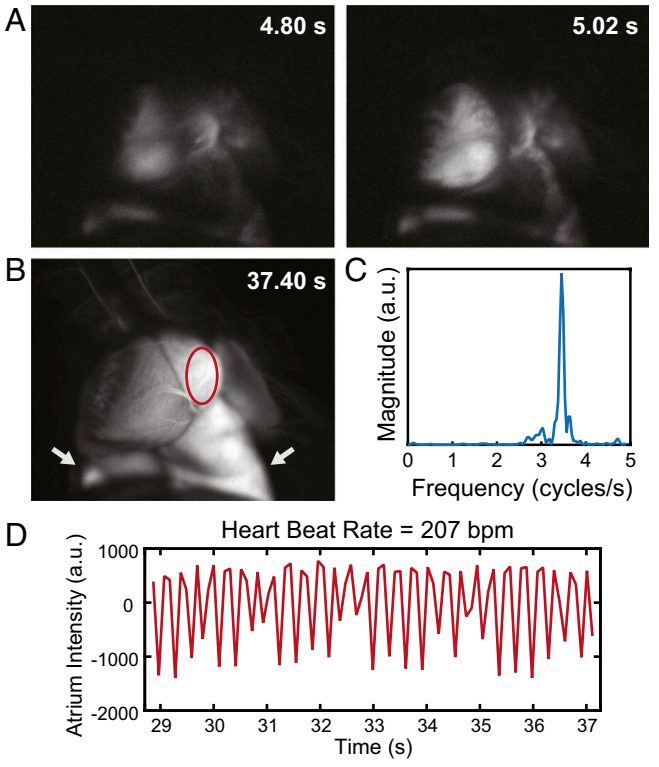

Fig. 4. High temporal resolution shown through ICG SWIR fluorescence angiography. Intravital SWIR fluorescence angiography was performed in a mouse heart at 9.17 frames per second using ICG for contrast, diffuse 808-nm excitation, and a 1,300-nm long-pass emission filter on an InGaAs SWIR camera (Movie S2). (*A*) Temporal resolution was sufficiently high to resolve the heartbeat of the mouse. (*B*) By tracking a region of interest within the atrium of the heart (red circle; lungs are also pictured and indicated with white arrows) and (*C*) taking the Fourier transform of (*D*) the intensity fluctuations, the heart rate was determined to be 207 beats per minute for the anesthetized mouse. Fluorescence tracking details and assignment of anatomical structures are in Fig. S5.

Using various long-pass filters across the SWIR, we find that lymph vessels and nodes are visible with ICG contrast up to ∼1,400 nm, at which point only the vessels and superficial nodes are visible and the signal of deeper lymph nodes becomes attenuated (Fig. S6*B*). Thus, for applications that are not contrast-limited, such as those with low background signal and/or high label specificity, it may be preferable to image ICG in the NIR or the shorter wavelengths of the SWIR, where signal attenuation is minimized.

These examples show the applicability of ICG SWIR imaging to fluorescence-guided surgery. ICG is bright enough to image in the SWIR at speeds sufficiently high for intraoperative imaging of dynamic or moving features, shown here in the heart, small intestine, and lymphatic system of a mouse. We show that the required speed for a given application can be balanced with the desired contrast by selecting the imaging wavelength; using the full SWIR regime enables the highest frame rates due to maximized signal from ICG, while imaging at the longest SWIR wavelengths can be used to improve contrast at the cost of speed. Thus, using an SWIR camera for detecting ICG provides a tunable platform for optimizing both contrast and speed in fluorescence-guided surgery.

Targeted SWIR Fluorescence Imaging in Vivo Using IRDye 800CW. The ease of molecular targeting is one of the major strengths of fluorescence imaging over other imaging modalities. We show here that straightforward conjugation chemistry can be used to perform targeted imaging in the SWIR using the NIR dye IRDye 800CW. We used a commercially available labeling kit to conjugate IRDye 800CW to the tumor-targeting antibody trastuzumab (62). We injected the dye–antibody conjugate into mouse models implanted with human BT474 breast cancer cells in the brain and noninvasively imaged the SWIR fluorescence emitted from the IRDye 800CW-labeled tumor through intact skin and skull. Subsequently, we injected IRDye 800CW conjugated to PEG, highlighting brain vasculature surrounding the tumor. A multicolor functional image of the brain was then generated by temporally resolving the two labels (i.e., by assigning different colors to the fluorescence signal before and after the addition of IRDye 800CW PEG) (Fig. S7) (63).

While targeted SWIR imaging has previously been hindered by the challenging preparation of targeted nanomaterials, the size-dependent delivery effects, and the unavailability of commercial solutions, the use of NIR dye labeling kits overcomes these barriers. NIR imaging of these readily available, targeted dyes has already shown promise for aiding cancer localization and intraoperative surgical margin assessment (64). Our results suggest that SWIR imaging of these NIR dyes could further benefit these applications by increasing the resolution of both fine and large structures, which may be overlapping, as this is a common occurrence in highly vascular malignant lesions.

Outlook. We show that established, commercially available NIR dyes, including the FDA-approved dye ICG, can be used to perform state of the art SWIR in vivo imaging, including intravital microscopy, noninvasive real-time imaging in blood and lymph vessels, imaging of hepatobiliary clearance, and molecularly targeted in vivo imaging. The advantages of SWIR imaging over NIR techniques, such as increased sensitivity, contrast, and resolution of fine anatomical structures, are, therefore, more readily available for increased adoption in preclinical and clinical imaging systems simply by switching the detection from conventional silicon-based NIR cameras to emerging, high-performance InGaAs SWIR cameras. While no FDA-approved fluorophores with peak emission in the SWIR yet exist, we show here that detecting the off-peak fluorescence of clinically accessible NIR dyes on SWIR detectors bears the potential for rapid translation of SWIR fluorescence imaging to humans in clinical applications.

Materials and Methods

Optical Characterization. *SI Materials and Methods* discusses characterization of dye absorption and emission spectra and quantum yield measurements as well as the dye brightness comparison.

In Vivo Imaging with ICG. All animal experiments were conducted in accordance with Public Health Service Policy on Humane Care of Laboratory Animals guidelines and were approved by the Institutional Animal Care and Use Committees of the Massachusetts Institute of Technology and Massachusetts General Hospital. No blinding or randomization was required for the animal studies. Before each imaging experiment, mice were anesthetized via i.p. injection of a ketamine/xylazine mixture (100 mg/kg ketamine and 10 mg/kg xylazine in saline), and sufficient depth of anesthesia was maintained, redosing with one-third the original dose in ketamine only as necessary. All tail vein injections were performed using a home-built catheter. The catheter was assembled by breaking the shaft of a 30-gauge needle into two pieces of equal length and reconnecting these pieces using plastic tubing. The hub of the needle was filled with saline solution and connected to a 1-mL syringe containing the desired contrast agent. Subsequently, the bevel of the needle was injected into the tail vein and fixed using tissue adhesive.

The in vivo imaging setup uses 50–70 mW/cm^2 of light from a 10-W, 808-nm laser (MLL-N-808; Opto Engine) coupled into a 910-μm core metal-cladded multimode fiber (MHP910L02; Thorlabs) and diffused through a ground glass plate (DG10-220-MD; Thorlabs). Fluorescence signal is directed from the imaging stage to the InGaAs SWIR camera (NIRvana 640; Princeton Instruments) using a 4-in. square first surface silver mirror (part no. 84448; Edmund Optics) and then filtered through various bandpass and long-pass emission filters incorporated into an exchangeable filter holder. Table S1 details the filters used for each image presented in this manuscript. Different objectives were used depending on the requirements of each application as detailed below. The InGaAs camera (NIRvana 640; Princeton Instruments) was cooled to −80 °C, the analog to digital (AD) conversion rate was set to 2 or 10 MHz, the gain was set to high, and different exposure times were used to achieve sufficient signal and/or frame rates (also detailed in Table S1). All images were background and blemish corrected within the LightField imaging software. The silicon camera (PIXIS 1024BR; Princeton Instruments) was cooled to −70 °C, the AD conversion rate was set to 2 MHz, the gain was set to high, and the exposure time was adjusted to achieve sufficient signal and/or frame rates (Table S1). ImageJ was used to average 10 frames for NIRvana and PIXIS images. Frame averaging was not used in videos unless otherwise noted. ImageJ was also used for all image measurements (pixel intensity average, SD, etc.).

SI Materials and Methods has detailed in vivo imaging procedures, including brain vasculature imaging, heart angiography, intravital brain imaging with ICG phospholipid micelles, ICG hepatobiliary clearance imaging, lymph node imaging, and IRDye 800CW tumor labeling and imaging.

Data Availability. The authors declare that all data supporting the findings of this study are available within the paper and in *SI Materials and Methods*.

Note. The results reported in this manuscript were initially posted by the authors on April 28, 2017, in the online archive, bioRxiv (65). During the manuscript review process, the authors became aware that ICG fluorescence in the SWIR was independently reported by another group in *PLoS One* on November 9, 2017 (66).

ACKNOWLEDGMENTS. We thank Sylvie Roberge for excellent technical support, Tulio Valdez for helpful discussions on imaging applications, and Ou Chen for help with spectroscopic characterization. We also thank Ellen Sletten and Christopher Rowlands for critical feedback on this manuscript. This work received support, in part, from NIH Grants CA080124 and CA208205 (to D. Fukumura and R.K.J.), CA096915 (to D. Fukumura), CA126642, CA165962, CA197743, and CA224173 (to R.K.J.), and Laser Biomedical Research Center Grant 9-P41-EB015871-26A1 (to M.G.B.); Department of Energy Office of Science, Basic Energy Sciences Award DE-FG02-07ER46454 (for spectroscopic characterization of dyes to J.R.C. and M.G.B.); Department of Defense Breast Cancer Research Program Innovator Award W81XWH-10-1-0016 (to R.K.J.); Harvard Ludwig Cancer Center (to R.K.J.); MIT-HCC (Massachusetts Institute of Technology–Harvard Cancer Center) Bridge grant (to R.K.J.); National Foundation for Cancer Research (R.K.J.); Massachusetts Institute of Technology Institute for Soldier Nanotechnologies Grant W911NF-13-D-0001 (to M.G.B.); and National Science Foundation Grant EECS-1449291 (to M.G.B.). This work was further conducted with government support under and awarded by

Department of Defense, Air Force Office of Scientific Research, National Defense Science and Engineering Graduate Fellowship 32 CFR 168a (to J.A.C.). D. Franke was supported by a fellowship from the Boehringer Ingelheim Fonds. C.F.P. was supported by a National Science Foundation Graduate Research Fellowship Program fellowship. M.D. was supported by National Heart, Lung, and Blood Institute of the NIH Award F31HL126449. O.T.B. was supported by a European Molecular Biology Organization long-term fellowship.

1. Sevick-Muraca EM (2012) Translation of near-infrared fluorescence imaging technologies: Emerging clinical applications. *Annu Rev Med* 63:217–231.
2. Zhu B, Sevick-Muraca EM (2015) A review of performance of near-infrared fluorescence imaging devices used in clinical studies. *Br J Radiol* 88:20140547.
3. Frangioni JV (2003) In vivo near-infrared fluorescence imaging. *Curr Opin Chem Biol* 7:626–634.
4. Vahrmeijer AL, Hutteman M, van der Vorst JR, van de Velde CJH, Frangioni JV (2013) Image-guided cancer surgery using near-infrared fluorescence. *Nat Rev Clin Oncol* 10: 507–518.
5. Marshall MV, et al. (2010) Near-infrared fluorescence imaging in humans with indocyanine green: A review and update. *Open Surg Oncol J* 2:12–25.
6. Alander JT, et al. (2012) A review of indocyanine green fluorescent imaging in surgery. *Int J Biomed Imaging* 2012:940585.
7. Koch M, Ntziachristos V (2016) Advancing surgical vision with fluorescence imaging. *Annu Rev Med* 67:153–164.
8. Polom K, et al. (2011) Current trends and emerging future of indocyanine green usage in surgery and oncology: A literature review. *Cancer* 117:4812–4822.
9. Te Velde EA, Veerman T, Subramaniam V, Ruers T (2010) The use of fluorescent dyes and probes in surgical oncology. *Eur J Surg Oncol* 36:6–15.
10. Rasmussen JC, Tan I-C, Marshall MV, Fife CE, Sevick-Muraca EM (2009) Lymphatic imaging in humans with near-infrared fluorescence. *Curr Opin Biotechnol* 20:74–82.
11. Daskalaki D, et al. (2014) Indocyanine green (ICG) fluorescent cholangiography during robotic cholecystectomy: Results of 184 consecutive cases in a single institution. *Surg Innov* 21:615–621.
12. Hong G, et al. (2012) Multifunctional in vivo vascular imaging using near-infrared II fluorescence. *Nat Med* 18:1841–1846.
13. Hong G, et al. (2014) Through-skull fluorescence imaging of the brain in a new near-infrared window. *Nat Photonics* 8:723–730.
14. Diao S, et al. (2015) Fluorescence imaging in vivo at wavelengths beyond 1500 nm. *Angew Chem Int Ed Engl* 54:14758–14762.
15. Bruns OT, et al. (2017) Next-generation *in vivo* optical imaging with short-wave infrared quantum dots. *Nat Biomed Eng* 1:0056.
16. Bashkatov AN, et al. (2005) Optical properties of human skin, subcutaneous and mucous tissues in the wavelength range from 400 to 2000 nm. *J Phys D Appl Phys* 38: 2543–2555.
17. Bashkatov AN, Genina EA, Tuchin VV (2011) Optical properties of skin, subcutaneous, and muscle tissues: A review. *J Innovative Opt Health Sci* 4:9–38.
18. Diao S, et al. (2015) Biological imaging without autofluorescence in the second near-infrared region. *Nano Res* 8:3027–3034.
19. Sordillo LA, Pu Y, Pratavieira S, Budansky Y, Alfano RR (2014) Deep optical imaging of tissue using the second and third near-infrared spectral windows. *J Biomed Opt* 19: 056004.
20. Zhang H, et al. (2016) Penetration depth of photons in biological tissues from hyperspectral imaging in shortwave infrared in transmission and reflection geometries. *J Biomed Opt* 21:126006.
21. Carr JA, Valdez TA, Bruns OT, Bawendi MG (2016) Using the shortwave infrared to image middle ear pathologies. *Proc Natl Acad Sci USA* 113:9989–9994.
22. US Department of State Directorate of Defense Trade Controls (2016) Commodity jurisdiction final determinations. Available at https://www.pmddtc.state.gov/commodity_jurisdiction/determinationAll.html. Accessed November 20, 2016.
23. Wilson RH, Nadeau KP, Jaworski FB, Tromberg BJ, Durkin AJ (2015) Review of short-wave infrared spectroscopy and imaging methods for biological tissue characterization. *J Biomed Opt* 20:030901.
24. Qian G, et al. (2008) Band gap tunable, donor–acceptor–donor charge-transfer heteroquinoid-based chromophores: Near infrared photoluminescence and electroluminescence. *Chem Mater* 20:6208–6216.
25. Qian G, et al. (2009) Simple and efficient near-infrared organic chromophores for light-emitting diodes with single electroluminescent emission above 1000 nm. *Adv Mater* 21:111–116.
26. Rogach AL, Eychmüller A, Hickey SG, Kershaw SV (2007) Infrared-emitting colloidal nanocrystals: Synthesis, assembly, spectroscopy, and applications. *Small* 3:536–557.
27. van Saders B, Al-Baroudi L, Tan MC, Riman RE (2013) Rare-earth doped particles with tunable infrared emissions for biomedical imaging. *Opt Mater Express* 3:566.
28. Antaris AL, et al. (2016) A small-molecule dye for NIR-II imaging. *Nat Mater* 15: 235–242.
29. Hong G, et al. (2014) Ultrafast fluorescence imaging in vivo with conjugated polymer fluorophores in the second near-infrared window. *Nat Commun* 5:4206.
30. Naczynski DJ, et al. (2013) Rare-earth-doped biological composites as in vivo shortwave infrared reporters. *Nat Commun* 4:2199.
31. Cosco ED, et al. (2017) Flavylium polymethine fluorophores for near- and shortwave infrared imaging. *Angew Chem Int Ed Engl* 56:13126–13129.
32. Tang R, et al. (2015) Tunable ultrasmall visible-to-extended near-infrared emitting silver sulfide quantum dots for integrin-targeted cancer imaging. *ACS Nano* 9: 220–230.
33. Hong G, et al. (2012) In vivo fluorescence imaging with Ag2S quantum dots in the second near-infrared region. *Angew Chem Int Ed Engl* 51:9818–9821.
34. Villa I, et al. (2015) 1.3 μm emitting SrF2:Nd3+ nanoparticles for high contrast in vivo imaging in the second biological window. *Nano Res* 8:649–665.
35. Tao Z, et al. (2013) Biological imaging using nanoparticles of small organic molecules with fluorescence emission at wavelengths longer than 1000 nm. *Angew Chem Int Ed Engl* 52:13002–13006.
36. Imamura Y, et al. (2016) Near-infrared emitting PbS quantum dots for in vivo fluorescence imaging of the thrombotic state in septic mouse brain. *Molecules* 21:1080.
37. Franke D, et al. (2016) Continuous injection synthesis of indium arsenide quantum dots emissive in the short-wavelength infrared. *Nat Commun* 7:12749.
38. Resch-Genger U, Grabolle M, Cavaliere-Jaricot S, Nitschke R, Nann T (2008) Quantum dots versus organic dyes as fluorescent labels. *Nat Methods* 5:763–775.
39. Gorka AP, Nani RR, Schnermann MJ (2015) Cyanine polyene reactivity: Scope and biomedical applications. *Org Biomol Chem* 13:7584–7598.
40. Nani RR, Shaum JB, Gorka AP, Schnermann MJ (2015) Electrophile-integrating Smiles rearrangement provides previously inaccessible C4′-*O*-alkyl heptamethine cyanine fluorophores. *Org Lett* 17:302–305.
41. Chen Y, et al. (2017) Shortwave infrared in vivo imaging with gold nanoclusters. *Nano Lett* 17:6330–6334.
42. Li-Cor (2018) IRDye 800CW NHS ester will label primary and secondary amines. Available at https://www.licor.com/bio/products/reagents/irdye/800cw/nhs_ester. Accessed January 11, 2018.
43. Akorn (2012) IC-Green (indocyanine green for injection, USP). Available at www.akorndirect.com/prod_detail.php?ndc=17478-701-02. Accessed January 11, 2018.
44. Philip R, Penzkofer A, Bäumler W, Szeimies RM, Abels C (1996) Absorption and fluorescence spectroscopic investigation of indocyanine green. *J Photochem Photobiol A* 96:137–148.
45. Condon E (1926) A theory of intensity distribution in band systems. *Phys Rev* 28: 1182–1201.
46. Yi X, Wang F, Qin W, Yang X, Yuan J (2014) Near-infrared fluorescent probes in cancer imaging and therapy: An emerging field. *Int J Nanomedicine* 9:1347–1365.
47. Würth C, Grabolle M, Pauli J, Spieles M, Resch-Genger U (2013) Relative and absolute determination of fluorescence quantum yields of transparent samples. *Nat Protoc* 8: 1535–1550.
48. Lim SJ, et al. (2015) Brightness-equalized quantum dots. *Nat Commun* 6:8210.
49. Landsman ML, Kwant G, Mook GA, Zijlstra WG (1976) Light-absorbing properties, stability, and spectral stabilization of indocyanine green. *J Appl Physiol* 40:575–583.
50. Leung K (2004) IRDye 800CW-human serum albumin. Available at https://www.ncbi.nlm.nih.gov/pubmed/20641282. Accessed December 21, 2016.
51. Laser Institute of America (2014) American national standard for safe use of lasers ANSI Z136.1-2014. Available at https://assets.lia.org/s3fs-public/pdf/ansi-standards/samples/ANSI%20Z136.1_sample.pdf. Accessed December 15, 2016.
52. Lim YT, et al. (2003) Selection of quantum dot wavelengths for biomedical assays and imaging. *Mol Imaging* 2:50–64.
53. Kraft JC, Ho RJY (2014) Interactions of indocyanine green and lipid in enhancing near-infrared fluorescence properties: The basis for near-infrared imaging *in vivo*. *Biochemistry* 53:1275–1283.
54. Paumgartner G, Probst P, Kraines R, Leevy CM (1970) Kinetics of indocyanine green removal from the blood. *Ann N Y Acad Sci* 170:134–147.
55. Meijer DKF, Weert B, Vermeer GA (1988) Pharmacokinetics of biliary excretion in man. VI. Indocyanine green. *Eur J Clin Pharmacol* 35:295–303.
56. Dashti R, Laakso A, Niemelä M, Porras M, Hernesniemi J (2011) Microscope integrated indocyanine green video-angiography in cerebrovascular surgery. *Acta Neurochir Suppl* 109:247–250.
57. Washington CW, et al. (2013) Comparing indocyanine green videoangiography to the gold standard of intraoperative digital subtraction angiography used in aneurysm surgery. *J Neurosurg* 118:420–427.
58. Dashti R, Laakso A, Niemelä M, Porras M, Hernesniemi J (2009) Microscope-integrated near-infrared indocyanine green videoangiography during surgery of intracranial aneurysms: The Helsinki experience. *Surg Neurol* 71:543–550.
59. Gruber A, Dorfer C, Standhardt H, Bavinzski G, Knosp E (2011) Prospective comparison of intraoperative vascular monitoring technologies during cerebral aneurysm surgery. *Neurosurgery* 68:657–673.
60. Sugie T, Ikeda T, Kawaguchi A, Shimizu A, Toi M (2016) Sentinel lymph node biopsy using indocyanine green fluorescence in early-stage breast cancer: A meta-analysis. *Int J Clin Oncol* 22:11–17.
61. Lee Z, Moore B, Giusto L, Eun DD (2015) Use of indocyanine green during robot-assisted ureteral reconstructions. *Eur Urol* 67:291–298.
62. Askoxylakis V, et al. (2015) Preclinical efficacy of ado-trastuzumab emtansine in the brain microenvironment. *J Natl Cancer Inst* 108:djv313.
63. Hillman EMC, Moore A (2007) All-optical anatomical co-registration for molecular imaging of small animals using dynamic contrast. *Nat Photonics* 1:526–530.
64. Rosenthal EL, et al. (2016) Successful translation of fluorescence navigation during oncologic surgery: A consensus report. *J Nucl Med* 57:144–150.
65. Carr JA, et al. (2017) Shortwave infrared fluorescence imaging with the clinically approved near-infrared dye indocyanine green. bioRxiv:10.1101/100768.
66. Starosolski Z, et al. (2017) Indocyanine green fluorescence in second near-infrared (NIR-II) window. *PLoS One* 12:e0187563.